JOURNAL OF AIRCRAFT
Vol. 38, No. 1, January–February 2001

Feedforward Piezoelectric Structural Control: An Application to Aircraft Cabin Noise Reduction

A. Grewal* and D. G. Zimcik†
National Research Council of Canada, Ottawa, Ontario K1A-0R6, Canada
and
B. Leigh‡
Bombardier Aerospace, Downsview, Ontario M3K-1Y5, Canada

The use of adaptive feedforward control within the active structural acoustic control framework was applied to the problem of propeller-induced noise and vibration reduction in the passenger cabin of the Bombardier (de Havilland) Dash-8 aircraft. Piezoceramic elements were used for structural actuation, and either vibration or acoustic sensing was employed. Actuators comprised of segmented piezoelectric elements were designed with the objective of reducing the noise and vibration levels at the propeller blade passage frequency (BPF) and the first harmonic. The actuator design objective was suppression of the operating deflection shapes (ODS) of the fuselage at the various frequencies by the judicious placement of piezoelectric elements. Using an actuator and sensor design optimized for the BPF together with vibration error sensing, the controller was successful in reducing interior noise in addition to vibration. Further improvement in noise reduction was obtained when acoustic error sensing was employed. Similar optimized designs for actuator and sensors were also found to exist at other frequencies, providing good noise and vibration attenuation. Furthermore, this strategy was successfully applied to noise reduction at two operating frequencies, where suppression of the ODSs at both the BPF and 2 × BPF was the objective.

Nomenclature

a_{m,k,i_a}	=	control filter forward coefficient for the mth control input caused by the kth reference signal, shifted i_a time steps
b_{m,p,i_b}	=	control filter recursive coefficient for the mth control input caused by the pth control input, shifted i_b time steps
c_{ℓ,m_1,j_c}	=	secondary path forward filter coefficient for the ℓth plant output caused by the m_1th input, shifted j_c time steps
d_{ℓ,q,j_d}	=	secondary path recursive filter coefficient for the ℓth plant output caused by the qth output, shifted j_d time steps
$\boldsymbol{d}$	=	vector of output signals as a result of the action of the reference inputs on the primary path
$\boldsymbol{e}$	=	residual error or output ($\boldsymbol{d}+\boldsymbol{y}$)
$\boldsymbol{G}_p$	=	primary path; transfer function matrix from reference (disturbance) input to error sensors
$\boldsymbol{G}_s$	=	secondary path; transfer function matrix from control input to error sensors
$\boldsymbol{H}$	=	feedforward controller
J	=	scalar cost function
$\boldsymbol{p}$	=	vector of sound pressure values
r_{ℓ,m,k,i_a}	=	kth reference signal filtered through the secondary path (from the mth input to the ℓth output)
s_{ℓ,m,p,i_b}	=	pth control input filtered through the secondary path (from the mth input to the ℓth output)
$\boldsymbol{u}$	=	vector of control input signals
$\boldsymbol{v}$	=	vector of voltages
$\boldsymbol{x}$	=	vector of reference input signals
$\boldsymbol{y}$	=	vector of output signals caused by the action of the controller
θ	=	generic filter coefficient
μ	=	convergence coefficient for steepest-descent method

Received 1 November 1999; revision received 10 July 2000; accepted for publication 10 July 2000.

*Research Officer, Structures, Materials, and Propulsion Laboratory, Institute for Aerospace Research; currently with Nortel Networks, P.O. Box 3511, station C, Ottawa, Ontario, K14 4H7. Member AIAA.

†Group Leader, Aeroacoustics and Structural Dynamics, Structures, Materials, and Propulsion Laboratory, Institute for Aerospace Research. Senior Member AIAA.

‡R&D Coordinator, Strategic Technologies, 123 Garratt Boulevard, MS N18-06. Member AIAA.

Introduction

THE noise levels in the passenger cabins of turbopropeller-driven aircraft, which result mainly from the excitation of the fuselage by the unsteady aerodynamic pressure field of the propellers, are typically higher than the noise levels in comparable turbofan-powered aircraft. This leads turboprop regional aircraft manufacturers to seek passive and active means of cabin noise and vibration reduction. Because the interior noise spectrum in these aircraft is dominated by tones occurring at integral multiples of the propeller blade passage frequency (BPF),[1] the reduction of interior noise and fuselage vibrations at these discrete frequencies provides a significant improvement to passenger comfort.

Passive techniques of noise and vibration reduction for this class of problem are generally not effective for a number of reasons. Because the excitation is usually neither broadband nor resonant, the addition of damping material does not have a major effect on noise and vibration levels. Moreover, sound absorption materials, for which the thickness must be at least comparable to the wavelength of the sound,[2] are ineffective at the low frequencies where propeller noise is significant (approximately 50–300 Hz). Structural damping enhancements such as constrained layer damping are also of limited use at low frequencies. Tuned vibration absorbers (TVA), which are located on fuselage frames and designed with a resonant frequency equal to that of the BPF thereby reducing the fuselage vibration and noise transmission, have also been considered for aircraft application. When subjected to a stationary harmonic disturbance, TVAs that are tuned accurately can be effective, but the variations in engine speed with operating conditions greatly limits their performance as a result of the required tradeoff between bandwidth and peak achievable attenuation.

Active noise control (ANC) of the aircraft cabin through the use of secondary acoustic sources has also been demonstrated.[3,4] Such

systems, which are presently offered by a number of turboprop aircraft manufacturers, incorporate a large number of trim-mounted speakers along with microphones and/or accelerometers to achieve noise reduction through destructive interference between the primary (disturbance) sources and the secondary (control) sources. Active structural acoustic control (ASAC) involves the use of structural actuators, such as piezoelectric devices or minishakers, and acoustic or structural sensors to accomplish noise attenuation. There is considerable interest in the ASAC approach because when compared to the ANC approach there tends to be a reduction in the number of actuators, less complexity in the control architecture, and a more global reduction in noise. One characteristic of ASAC is that it involves reducing the transmission of noise (i.e., before it enters the cabin). This is consistent with the well-accepted rule that treating noise at or close to its source yields superior performance compared to treating the problem further down the transmission path. The resulting system is generally simpler with fewer actuator and sensors because they are required only in the propeller footprint area.[5,6]

Background

The use of piezoelectric elements as structural actuators has a number of benefits as a result of their high bandwidth, low weight, and distributed actuation property. The latter property is of particular interest because of the possibility of selectively imparting control authority over those structural modes that interact strongly with the acoustics of the aircraft interior (i.e., radiating modes). The major disadvantage of piezoelectric materials is their high-voltage requirement. However, the required voltage can be reduced considerably by constructing a stack of thinner piezoelectric elements.

The feasibility of using piezoelectric actuators and structural sensors has previously been experimentally investigated and established on a full-scale Bombardier (de Havilland) Dash-8 Series 100 fuselage using multiple piezoelectric elements connected to form a single actuator located in the plane of the propeller.[7] Noise attenuation of nearly 5 dB at the control frequency was achieved when sensing of the fuselage radial acceleration was employed together with a classical second-order single-input, single-output compensator. A single speaker was used as the sound source in this work. The Dash-8 Series 100 fuselage is shown in Fig. 1.

In a subsequent study the preceding work was extended by employing multiple piezoelectric actuators along with a multiloop feedback control system on the Dash-8 fuselage.[8] Classical compensators were also used for each of the dominant loops of the system. A more sophisticated sound source consisting of a speaker-ring with four loudspeakers was used. Using this system, the in-flight magnitude and phase distribution of noise on the exterior of the fuselage was simulated in the neighborhood of the propeller plane. At the BPF (61 Hz) interior noise attenuation as high as 14.8 dB and a peak vibration reduction in excess of 20 dB were achieved.

In the present investigation the emphasis is placed on the use of adaptive feedforward control, the configuring of piezoelectric actuators for control at multiple frequencies, and on comparing the performance obtained with acoustic vs structural error sensing. The paper is organized as follows. First, the salient aspects of the theory of multi-input, multi-output (MIMO) filtered-u recursive-least-mean-squares (RLMS) adaptive feedforward control are reviewed. Next, details of the experimental setup, including control implementation, the speaker-ring noise simulation, and the actuator and sensor design approaches are presented. Finally, the various experimental results are presented and discussed.

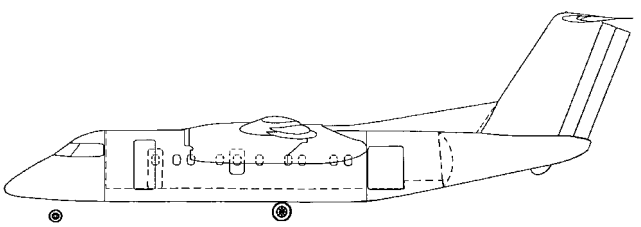

Fig. 1 The de Havilland Dash-8 S-100/200 aircraft.

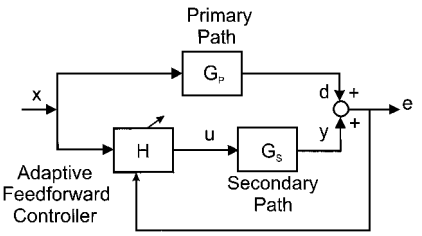

Fig. 2 Block diagram for adaptive feedforward control.

MIMO Filtered-u RLMS Control

The filtered-u RLMS adaptive feedforward scheme is an extension of the filtered-x scheme to cases when infinite-impulse response (IIR) or recursive digital filters are used for the control filter and to model the secondary path. The MIMO version of the filtered-u RLMS adaptive feedforward control algorithm[9] is implemented experimentally in this study. This control method requires that the transfer functions between the control actuators and the error sensors (i.e., the secondary path) be estimated. Both on-line and off-line approaches to the estimation of these transfer functions have been developed.

The structure of a generic adaptive feedforward controller together with the plant is shown in Fig. 2. The vector of K reference input signals $\boldsymbol{x}$ passes through the transfer function matrix $\boldsymbol{G}_p$, which is also referred to as the primary path of the system, producing a vector of L disturbance signals $\boldsymbol{d}$. A secondary path $\boldsymbol{G}_s$ between M actuators inputs $\boldsymbol{u}$ and the vector of L outputs $\boldsymbol{y}$ is also present. The residual error signal as measured by the L error sensors is denoted by $\boldsymbol{e}$, the complex vector sum of $\boldsymbol{d}$ and $\boldsymbol{y}$. A feedforward controller denoted by $\boldsymbol{H}$, which is adapted by the error $\boldsymbol{e}$, is used to filter the reference input signal to produce a control signal, which is applied to the actuators. The overall objective is to design this feedforward controller such that the magnitude of $\boldsymbol{e}$ is kept as small as possible.

The secondary path is assumed to be represented adequately in the discrete time domain by an IIR filter with N_c forward and N_d recursive coefficients, i.e.,

$$y_\ell^n = \sum_{m_1=1}^{M} \sum_{j_c=0}^{N_c-1} c_{\ell,m_1,j_c}^n u_{m_1}^{n-j_c} + \sum_{q=1}^{L} \sum_{j_d=1}^{N_d} d_{\ell,q,j_d}^n y_q^{n-j_d} \tag{1}$$

where the superscripts (i.e., $n, n-j_c, n-j_d$) indicate the sample period; $\ell = 1, \ldots, L$ is the element of the sensor output vector; and c_{ℓ,m_1,j_c} is the forward filter coefficient for the ℓth plant output as a result of the m_1th input, shifted j_c time steps. The recursive filter coefficient d_{ℓ,q,j_d} is defined as the coefficient for the ℓth plant output caused by the qth output, shifted j_d time steps.

For generality, the control filter is also chosen to be an IIR filter with N_a forward and N_b recursive coefficients, i.e.,

$$u_m^n = \sum_{k=1}^{K} \sum_{i_a=0}^{N_a-1} a_{m,k,i_a}^n x_k^{n-i_a} + \sum_{p=1}^{M} \sum_{i_b=1}^{N_b} b_{m,p,i_b}^n u_p^{n-i_b} \tag{2}$$

A finite-impulse response (FIR) filter can be specified by simply choosing $N_b = 0$. Here a_{m,k,i_a} is the forward coefficient for the mth control input caused by the kth reference signal, shifted i_a time steps, whereas b_{m,p,i_b} is the recursive coefficient for the mth control input caused by the pth control input, shifted i_b time steps.

At present all coefficients for the secondary path model and the control filter are assumed to be time varying. The two defining characteristics of the LMS algorithm are the approximation of the expected values of signals by their instantaneous values and the use of the steepest-descent method to update the filter coefficients such that the cost function approaches a minimum,[10] i.e.,

$$\theta^{n+1} = \theta^n - \frac{\mu}{2} \frac{\partial J(n)}{\partial \theta} \tag{3}$$

where $J(n)$ is the instantaneous value of the cost function to be minimized, which is simply the sum of the squares of the L error signals, i.e.,

$$J(n) = \sum_{\ell=1}^{L} e_\ell^2(n) \tag{4}$$

The presence of the secondary path results in a modified version of the standard LMS algorithm, which is commonly referred to as the filtered-u RLMS algorithm. The resulting update algorithm for the control filter coefficients given by filtered-u RLMS algorithm is found to be

$$a_{m,k,i_a}^{n+1} = a_{m,k,i_a}^{n} - \mu \sum_{\ell=1}^{L} e_\ell(n) r_{\ell,m,k,i_a}^{n}$$

$$b_{m,p,i_b}^{n+1} = b_{m,p,i_b}^{n} - \mu \sum_{\ell=1}^{L} e_\ell(n) s_{\ell,m,p,i_b}^{n} \tag{5}$$

where r_{ℓ,m,k,i_a} and s_{ℓ,m,p,i_b} are the kth reference signal and pth control input, respectively, filtered through the secondary path (from the mth input to the ℓth output), i.e.,

$$r_{\ell,m,k,i_a}^{n} = \sum_{j_c=0}^{N_c-1} c_{\ell,m,j_c}^{n} x_k^{n-i_a-j_c} + \sum_{q=1}^{L}\sum_{j_d=1}^{N_d} d_{\ell,q,j_d}^{n} r_{q,m,k,i_a}^{n-j_d}$$

$$s_{\ell,m,p,i_b}^{n} = \sum_{j_c=0}^{N_c-1} c_{\ell,m,j_c}^{n} u_p^{n-i_b-j_c} + \sum_{q=1}^{L}\sum_{j_d=1}^{N_d} d_{\ell,q,j_d}^{n} s_{q,m,p,i_b}^{n-j_d} \tag{6}$$

In each of the preceding equations, in addition to the normal delay associated with an IIR filter there also exists a delay associated with the coefficients of the forward or recursive portions, i.e., i_a or i_b. The requirement of filtering the reference and control signals through the actual secondary path is an impractical task. However, if available, a filter that represents an estimate of the secondary path, given by the coefficient arrays $\hat{\boldsymbol{C}}$ and $\hat{\boldsymbol{D}}$, can be used in place of the secondary path itself. This estimate can be obtained by a number of on-line or off-line techniques. One such approach, shown in Fig. 3, uses the standard RLMS algorithm to produce this estimate.[4] The on-line identification approach is shown here although the off-line procedure simply involves applying the method in the absence of the control filter. A random signal $\boldsymbol{v}$ is applied to both the secondary path and the digital filter given by $\hat{\boldsymbol{C}}$ and $\hat{\boldsymbol{D}}$. The error between the plant and its estimate $\boldsymbol{e}$ is used to adapt the filter coefficients in a manner identical to that described earlier. In reference to Eq. (1), the update algorithm for the filter coefficients of the estimated secondary path is given by

$$\hat{c}_{\ell,m_1,j_c}^{n+1} = \hat{c}_{\ell,m_1,j_c}^{n} - \tilde{\mu}\tilde{e}_\ell(n)\tilde{x}_{m_1}^{n-j_c}$$

$$\hat{d}_{\ell,q,j_d}^{n+1} = \hat{d}_{\ell,q,j_d}^{n} - \tilde{\mu}\tilde{e}_\ell(n)\tilde{y}_q^{n-j_d} \tag{7}$$

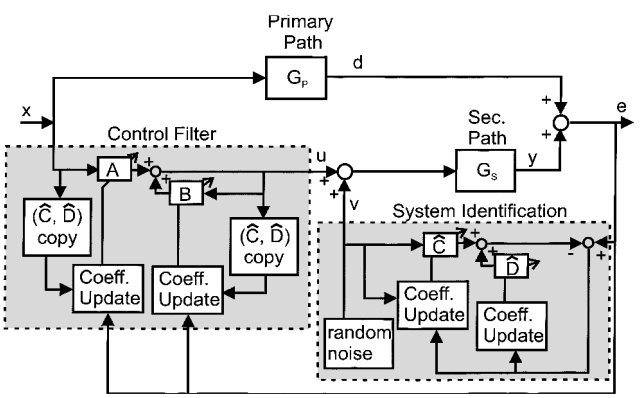

Fig. 3 Filtered-u RLMS adaptive control with plant identification.

where the tilde is used to denote the values of variables during the system identification process. The identification process can occur in parallel with the control process although achieved performance may be very sensitive to the strength of the training random signal. The selection of a level acceptably high for good system identification in the presence of the primary disturbance, but acceptably low in terms of the residual noise or vibration level, can prove to be difficult in some cases. Another factor is the demanding computational resources required in implementing simultaneous system identification and control, especially if the disturbance frequencies are high.

A straightforward implementation of Eqs. (2), (5), and (6) also results in a very large computational burden. Under the assumption of slowly varying plant model coefficients, in the case of on-line plant identification or stationary plant model coefficients, which occurs if off-line identification is used, and zero initial conditions, the generation of the filtered control and reference signals is simplified considerably. Under these assumptions Eq. (6) reduces to

$$r_{\ell,m,k,i_a}^{n} = r_{\ell,m,k,i_a-1}^{n-1}, \qquad \forall i_a = 1, \ldots, \max(N_a - 1, N_d)$$

$$r_{\ell,m,k,i_a}^{n} = \sum_{j_c=0}^{N_c-1} c_{\ell,m,j_c}^{n} x_k^{n-i_a-j_c} + \sum_{q=1}^{L}\sum_{j_d=1}^{N_d} d_{\ell,q,j_d}^{n} r_{q,m,k,i_a}^{n-j_d} \qquad \forall i_a = 0$$

$$s_{\ell,m,p,i_b}^{n} = s_{\ell,m,p,i_b-1}^{n-1}, \qquad \forall i_b = 2, \ldots, \max(N_b, N_d + 1)$$

$$s_{\ell,m,p,i_b}^{n} = \sum_{j_c=0}^{N_c-1} c_{\ell,m,j_c}^{n} u_p^{n-i_b-j_c} + \sum_{q=1}^{L}\sum_{j_d=1}^{N_d} d_{\ell,q,j_d}^{n} s_{q,m,p,i_b}^{n-j_d} \qquad \forall i_b = 1 \tag{8}$$

Thus, except for those filtered values associated with $i_a = 0$ and $i_b = 1$, that is those associated with the latest values of the signals for a given j_c and j_d, the quantities r_{ℓ,m,k,i_a} and s_{ℓ,m,p,i_b} can be obtained by a simple shifting process. This results in a considerable reduction in the real-time computational requirement. Of the three major steps, i.e., 1) computing the control signals, 2) computing the filtered reference and filtered control signals, and 3) updating the control filter coefficients, the most burdensome by far is the second step. As an illustration, assume for the moment that $N_a = N_b = N_c = N_d \equiv N$. Then, prior to the preceding simplification, the computation of the filtered reference and control signals required approximately N^2 floating point operations (FLOPs) for each control input m, error output ℓ, and reference input k. The aforementioned simplification reduced this requirement to N FLOPs and N shift operations, which can be programmed very efficiently on most modern digital signal processors (DSPs) through the use of the circular addressing mode.[11]

Experimental Implementation and Setup

A schematic diagram of the experimental setup used in this investigation is given in Fig. 4.

Control Implementation

The controllers described earlier were implemented on a DSP system consisting of a Spectrum QPC40 processor board equipped with a single Texas Instruments TMS320C40 processor. I/O was provided on a separate board with 16 channels of 12-bit analog inputs and 8 channels of 12-bit analog outputs. Communication between the processor and I/O board was achieved via a high-speed 16-bit interface. Other features of the I/O board include programmable input gain, a maximum sample rate of 25 kHz (with all channels in use), and on-board third-order Butterworth anti-aliasing and reconstruction low-pass filters for all input and output channels (with −18 dB/octave roll off).

Even with the simplifications discussed earlier, the relative complexity of the MIMO filtered-u RLMS algorithm required that mixed

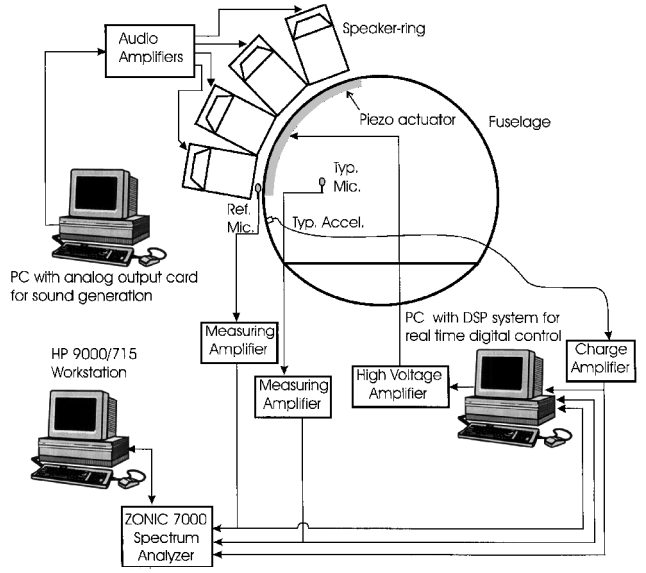

Fig. 4 Schematic of the control system and experimental setup.

C/Assembler language code be used. This allowed for the use of a number of low-level programming techniques such as the use of parallel instructions and the circular addressing mode for the implementation of the time critical aspects of the algorithm. These operations include the filter implementation, updating of the input and control vectors, and updating of the filtered input and control signals. The outputs of the controller were amplified by a pair of dual-channel Trek model 50/750 high-voltage amplifiers designed specifically for driving active loads.

Test Article

The test article was a full-sized Bombardier (de Havilland) Dash-8 Series 100/200 fuselage without horizontal lifting surfaces. The cargo and pilot's bulkheads as well as the floor were present in the interior although the trim panels and seats were removed. The fuselage rests on a cradle-fitted trailer except during testing when an overhead crane raised the fuselage using steel cables, which were attached to the fuselage at the wing-fuselage interface. This arrangement was deemed to subject the fuselage to support conditions that resemble steady level flight. The fuselage was placed in a high bay measuring approximately 21 m (70 ft) × 14 m (45 ft) with a height of 11 m (35 ft). The temperature in the high bay was maintained at approximately 20°C at ambient atmospheric pressure.

Noise Source

The port-side exterior propeller pressure field was simulated using the sound field generated by a speaker-ring with four 12-in. (0.5 cm) loudspeaker units, each with a rated power of 200 W. Each unit had two sections, a sealed plywood enclosure that formed the speaker box and a horn section with an opening that measured 76 cm (30 in.) × 61 cm (24 in.). The speaker-ring covered an arc of approximately 100 deg on the fuselage and was maintained at distance of approximately 5 cm from the fuselage surface to allow for the blending of the sound from the individual speakers. The four individual waveforms were synthesized by a National Instruments AT-AO-10 analog output card and amplified using a pair of Ashly MFA-8000 dual-channel power amplifiers.

The exterior propeller pressure field at the surface of the fuselage has been simulated numerically for the Series 100 aircraft by the propeller manufacturer. The objective of using the present speaker-ring was not to recreate the entire propeller field, but rather to represent its phase and magnitude characteristics over the key region close to the propeller plane. It can be extended in the future to provide a simulation of a larger portion of the propeller field.

Because of the blending of sound fields from each speaker, it was not possible to use directly the desired magnitude and phase at the regions of the fuselage located adjacent to the four speakers as the magnitudes and phases of the waveforms supplied to each speaker. The approach employed here was to determine the transfer function matrix between input voltages to the four speakers and the resulting sound field at a number of distinct locations. The relationship between the vector of speaker input voltages $\boldsymbol{v}$ and the resulting sound pressure field measured at a number of distinct locations $\boldsymbol{p}$ is given by

$$\boldsymbol{p} = \boldsymbol{G}\boldsymbol{v} \tag{9}$$

The transfer matrix $\boldsymbol{G}$ is a complex matrix whose columns can be determined experimentally simply by measuring the vector of complex sound pressure values $\boldsymbol{p}$ as a result of each of the four unit basis vectors of speaker input voltages, i.e.,

$$\boldsymbol{v} = \begin{Bmatrix} 1 \\ 0 \\ 0 \\ 0 \end{Bmatrix}, \begin{Bmatrix} 0 \\ 1 \\ 0 \\ 0 \end{Bmatrix}, \begin{Bmatrix} 0 \\ 0 \\ 1 \\ 0 \end{Bmatrix}, \begin{Bmatrix} 0 \\ 0 \\ 0 \\ 1 \end{Bmatrix} \tag{10}$$

Alternately, any set of four independent vectors can be employed, in which case $\boldsymbol{G}$ is computed by

$$\boldsymbol{G} = \boldsymbol{P}\boldsymbol{V}^{-1} \tag{11}$$

where $\boldsymbol{V}$ is the full rank matrix formed by the four independent vectors of voltages and $\boldsymbol{P}$ is the matrix formed by the resulting vectors of pressures.

Next, the required vector of voltages $\boldsymbol{v}_r$, which minimizes the squared error between the desired $\boldsymbol{p}_d$ and achieved pressure fields, can be determined. Provided that the columns of $\boldsymbol{G}$ are independent, this vector is given by

$$\boldsymbol{v}_r = (\boldsymbol{G}^H\boldsymbol{G})^{-1}\boldsymbol{G}^H\boldsymbol{p}_d \tag{12}$$

where the superscript $\boldsymbol{H}$ denotes the Hermitian (complex-conjugate) transpose of the matrix.

Using this approach, the desired and achieved relative magnitude and phase of the propeller field at fuselage exterior were found to be in good agreement. The noise generation system is discussed in greater detail in Refs. 8 and 12.

Actuator and Sensor Design Approach

The interaction between piezoelectric actuators and the structures to which they are bonded is of considerable interest, with numerous studies reported on beams, plates, and cylindrical shells. One of the earliest studies on piezoelectric actuators bonded onto beams showed that as the bonding layer became thinner and stiffer the loading transfer between actuator and substructure occurred over a increasingly small region at the two ends of the actuator element.[13] Therefore when a series of elements are bonded close together and subjected to the same electrical field, they will behave as a single long actuator, with only the outer ends of the first and last elements having a loading effect; the work done by and hence control contribution of the adjoining ends of neighboring piezoelectric elements tend to cancel. The requirements for this are that the distance between neighboring elements be considerably less than the lengths of individual elements. This result can be used to design actuators that selectively impart control authority over vibrational modes.

In the present work 199 piezoelectric elements each measuring $1 \times 1 \times \frac{1}{4}$ in. (25.4 × 25.4 × 6.4 mm) were bonded onto three adjacent fuselage frames on the port side of the aircraft. A distance of $\frac{1}{8}$ in. (3.2 mm) was maintained between neighboring elements. The elements are a Type I d_{31}-mode ceramic designated BM400 by the supplier, Sensor Technology Limited of Collingwood, Ontario, Canada. The material characteristics of BM400 are given in Table 1. The electrical power cables for the piezoelectric elements were configured in such a way that power to individual elements could be disconnected. As a result, there is a great deal of flexibility in quickly reconfiguring the coverage and the actual number of actuators.

There have been numerous model-based approaches for optimizing the location of positioning of piezoelectric actuators on simple structures such as beams and plates. For obvious reasons these approaches are not applicable to complex structures such as aircraft fuselages. In more complex structures the optimal positioning of actuators for noise and vibration control is often determined using experimental data together with a combinatorial optimization scheme.[14] In the present case a more physical approach was followed; the vibration patterns or operating deflection shapes of the fuselage were used to determine the specific elements to be included in the actuators, in particular the circumferential limits of each actuator.

The one-sided or asymmetric actuation of a structure such as an aircraft fuselage by bonded piezoelectric elements will produce both flexural and in-plane vibration. For the case of noise transmission into an aircraft cabin, flexural vibrations are of greater significance as a result of their ability to couple with acoustic waves. In the case of flexural vibration, the predominant actuation mechanism for a rectangular piezoelectric actuator is the application of bending moments at its ends on the host structure. This is true of both monolithic and segmented piezoelectric actuators. With this in mind, a segmented actuator with all of its elements connected in phase should be positioned such that its ends coincide with regions of high (and opposite) angular rotation in order to have high control authority over that particular mode. If the ends are located in regions of high displacement (and hence low rotation) or if the rotations at the ends are nearly equal, low control authority over that mode results. More details on the actuator design methodology can be found in Refs. 8 and 12.

For ASAC applications care must be taken to ensure that the structural sensor is measuring a quantity well correlated with the sound levels to be reduced. In a fashion analogous to the design of actuators, piezoelectric material can also be used to selectively sense certain modes of vibration. Polyvinylidene film has been used extensively for this application. When using discrete sensors, the use of a weighted average of sensor signals can produce a similar effect. This ensures that the average vibration over the critical region is measured and reduced by the control system. In doing so the volume velocity strength of the residual vibration pattern will decrease, resulting in lower interior noise levels.

Because of the relatively low frequencies of interest here (i.e., up to 140 Hz) and the relatively large region of high acoustic pressure on the fuselage exterior, the dominant vibrational modes will be of relatively low order. Furthermore, in most aircraft propeller noise problems it is the low-order, volumetric structural modes that are responsible for much of the noise transmission. Therefore, by designing sensors and actuators that are tailored to effectively detect and control these modes good vibration and noise reduction performance should occur.

Table 1 Material characteristics of BM400 piezoelectric

Property	Value
Charge constant, d_{31}	-115×10^{-12} C/N
Elastic compliance, S_{11}^{E}	12.5×10^{-12} m^2/N
Mass density, ρ	7.6 g/cm^3

Experimental Results

The first case explored was control at 61 Hz (910 rpm, BPF) with accelerometer error sensing. Based on the actuator design approach discussed earlier and the measured deflection pattern at 61 Hz, which is shown in Fig. 5, three piezoelectric actuators were designed by connecting all of the elements located between adjacent nodal lines of the deflection pattern (i.e., points I and II) at each frame in parallel. This is referred to as configuration A and is also indicated on Fig. 6, where elements p10–p49 are activated. Actual available piezoelectric coverage extended from points I to III. Figure 7 shows a side view of the fuselage with the axial locations of the piezoelectric elements, accelerometers and microphones indicated. Four accelerometers were placed over the region of high open-loop vibration (i.e., between points I and II on Fig. 5) at the three axial locations where piezoelectric elements were bonded. The signals from accelerometers a1 to a4, a5 to a8, and a9 to a12 were summed respectively to effectively create three sensors (see Fig. 6). An IIR filter with 15 forward and 14 recursive filter coefficients was used to model the secondary path using off-line RLMS system identification. A band-limited random signal between 55 and 75 Hz was used for plant identification. The control filter was chosen to be a FIR filter with 15 coefficients and was implemented at a sampling rate of

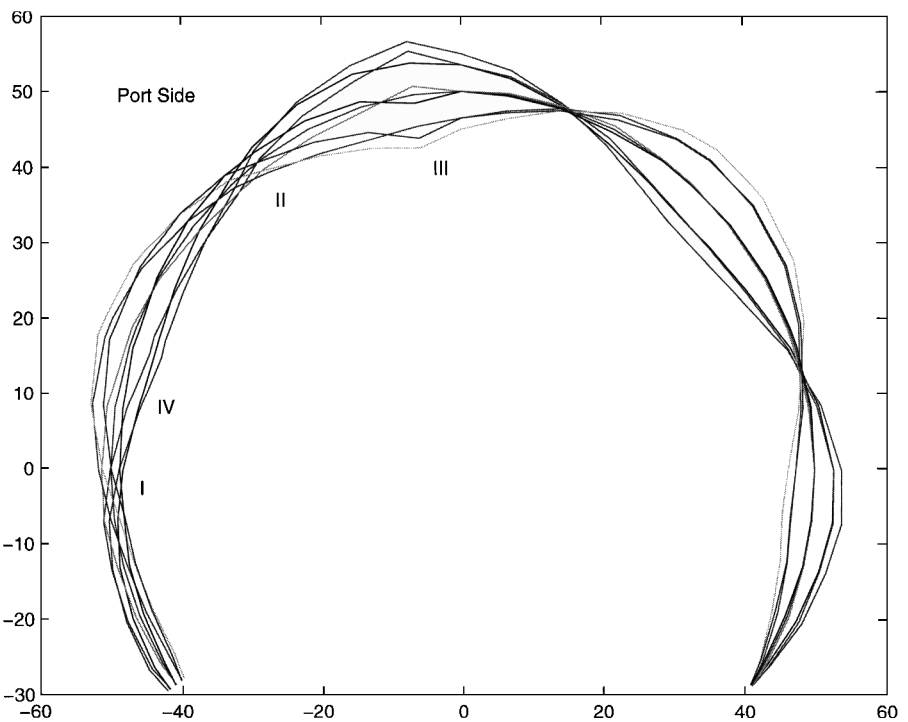

Fig. 5 Measured operating deflection shape caused by simulated propeller noise, BPF, 910 rpm (61 Hz). The lines represent fuselage deflections at fixed time interval over a single period of oscillation.

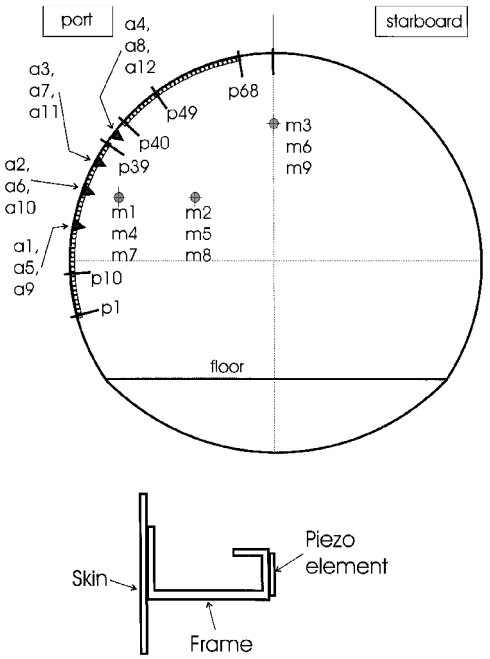

Fig. 6 Section through frame 1, showing microphone (m1 to m9), actuator (p1 to p68), and accelerometer location (a1 to a12) for configuration A. Also shown is the piezo location on the fuselage frame.

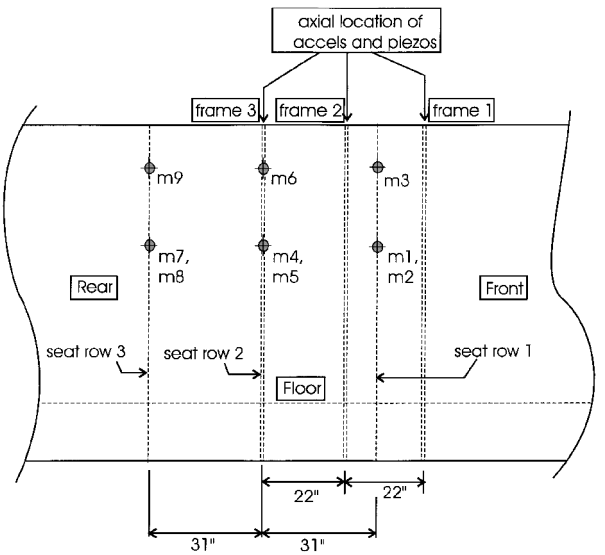

Fig. 7 Side view of instrumented section, showing microphone locations (m1 to m9) and axial locations of accelerometers and actuators.

2 kHz. The reductions in the vibration levels for the 12 accelerometer locations as well as for the true sensed variables (i.e., the three average acceleration values) are given in Table 2. The attenuation values quoted are in decibels computed as follows:

$$\text{Attenuation (dB)} = 20 \log_{10}(x_o/x_c) \tag{13}$$

where x_o and x_c are the open- and closed-loop measured responses (acoustic or structural), respectively. Positive attenuation values indicate reduced levels of noise or vibration, whereas negative values indicate increased levels. A good measure of overall vibration suppression performance is given by the attenuation of the rms of all accelerometers, which in this case is 10.2 dB. The spectra for the control-on and control-off data for a typical accelerometer (number a11) are shown in Fig. 8. The spectra are presented in decibels with respect to an arbitrary reference value to avoid revealing sensitive proprietary information. The principal objective of this figure is

Table 2 Vibration attenuation in decibels at 61 Hz, vibration sensing, configuration A

Accelerometer	Location	Attenuation, dB
a1	Lower, frame 1	5
a2	Frame 1	18
a3	Frame 1	19
a4	Upper, frame 1	11
Sensor I (average: a1–a4)	——	39
a5	Lower, frame 2	5
a6	Frame 2	16
a7	Frame 2	14
a8	Upper, frame 2	7
Sensor II (average: a5–a8)	——	42
a9	Lower, frame 3	8
a10	Frame 3	13
a11	Frame 3	21
a12	Upper, frame 3	4
Sensor III (average: a9–a12)	——	33
rms: a1–a12	——	10.2

Table 3 Interior noise attenuation in decibels at 61 Hz, actuator configurations A and B

Microphone	Location	Configuration A (accelerometer sensing)	Configuration B (microphone sensing)
m1	Row 1, window seat	2	1
m2	Row 1, aisle seat	24	9
m3	Row 1, standing aisle	6	18
m4	Row 2, window seat	10	11
m5	Row 2, aisle seat	9	19
m6	Row 2, standing aisle	7	20
m7	Row 3, window seat	14	7
m8	Row 3, aisle seat	10	13
m9	Row 3, standing aisle	6	13
Average: m1–m9	——	9.8	12.3
rms: m1–m9	——	7.2	12.5

to illustrate the relative differences between open- and closed-loop spectra.

For monitoring the noise reduction performance, a total of nine microphones (see Figs. 6 and 7) were positioned at the seated height for passengers in the two port side seats and at the aisle center standing height for seat rows 1, 2, and 3. The tone level attenuation data for the configuration A together with the results for configuration B, which used microphone error sensing (to be discussed later), are presented in Table 3. The reduction in tone level was quite global in nature, with all of the microphone positions exhibiting reductions. The average and rms tone-level reductions over all nine microphones were 10 and 7 dB, respectively, in this case. This type of global performance is typical of ASAC-based systems as opposed to noise control systems that employ acoustic secondary sources, which often exhibit only local noise reduction. The control-on and control-off noise level spectra for a typical microphone location (m2), namely the aisle seat in row 1, for the vibration error sensing case are presented in Fig. 9 and reveal some control spillover into other frequencies. Note that as was the case with the vibration spectra, the reference acoustic pressure for the decibel representation is unspecified to protect proprietary information.

In configuration B the three microphones located in the second seat row (i.e., m4 to m6) were used are error sensors, although the actuator arrangement was identical to configuration A. The remaining six microphones were used only in monitoring noise control performance. In this case the noise control performance at the BPF was superior to the preceding case (configuration A). The control microphones experienced tone-level reductions of 11, 19, and 20 dB, respectively, while the average and rms reductions over all microphones were 12.3 and 12.5 dB, respectively (see Table 3). The significantly better noise control performance of the system with

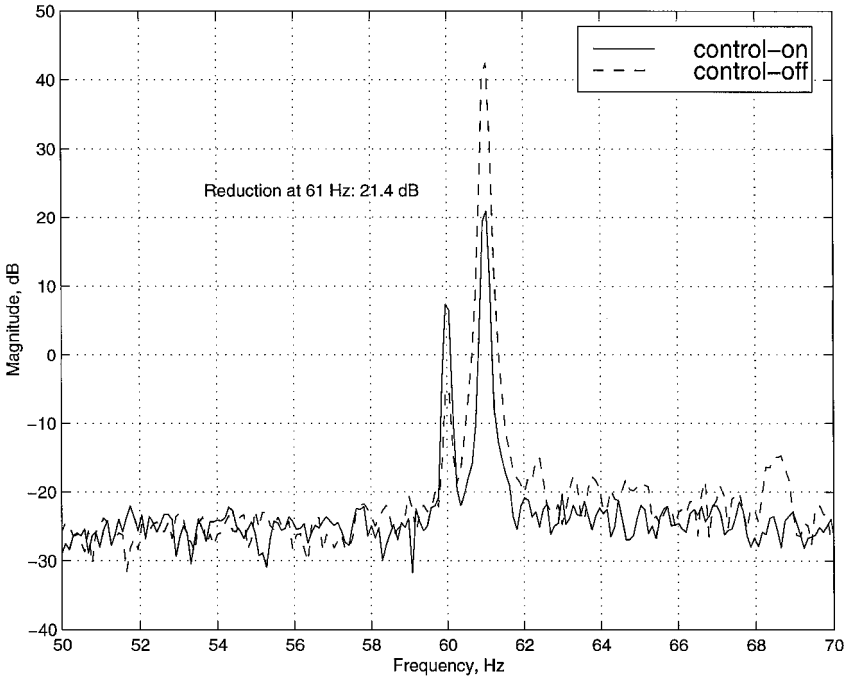

Fig. 8 Acceleration spectra for accelerometer a11, feedforward control, vibration sensing, 61 Hz.

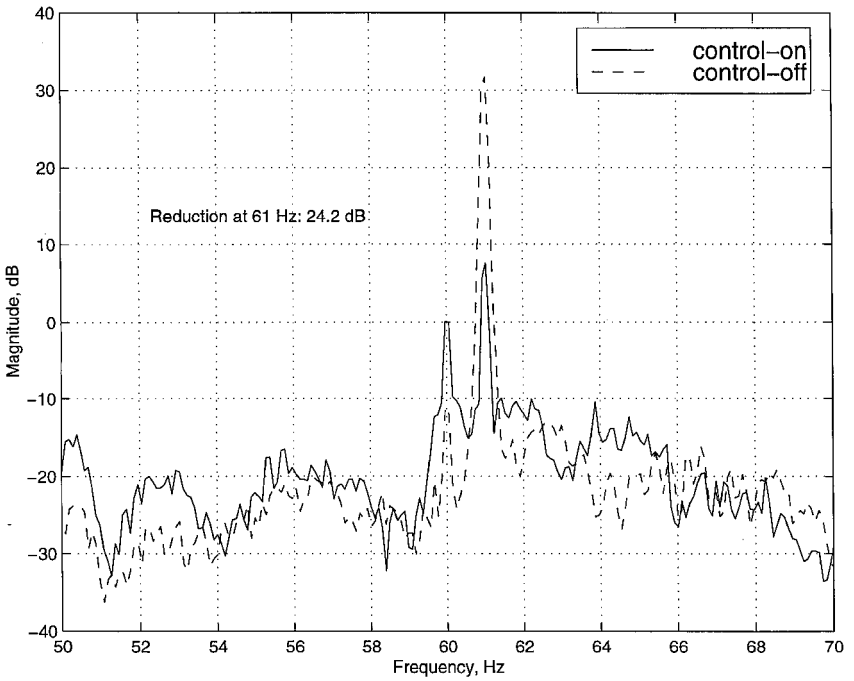

Fig. 9 Sound-level spectra for row 1 aisle seat (microphone m2), feedforward control, vibration sensing, 61 Hz.

microphone sensing in comparison to the system that employed accelerometer sensing is not surprising. Rather what is somewhat surprising is the excellent noise control performance using structural sensing, obtained through the judicious placement of accelerometers and the appropriate averaging of their signals. This is possible because of the relatively few structural and acoustic modes present in the response of the system at the BPF (61 Hz), their low order and hence their relatively simple coupling. Thus by suppressing the dominant structural mode, significant noise reduction also resulted.

For most turboprop aircraft the dominant tone in the multitonal interior sound field in terms of sound pressure level is the BPF. In some aircraft, when an A-weighting is applied to help account for the spectral sensitivity of the human ear, the magnitude of the first harmonic rivals that of the fundamental. Typically, the magnitudes of the higher harmonics are significantly lower than those of the fundamental and first harmonic. Furthermore, the transmission of the noise field at the higher harmonics is adequately reduced using various passive means. However, it is usually important that the active noise control system be capable of reducing the noise as a result of the first harmonic of the blade passage frequency, i.e., $2 \times$ BPF, in addition to the fundamental tone. Therefore, the performance of a given actuator/sensor configuration at the first harmonic of the BPF was also evaluated. The vibration suppression performance of configuration A at $2 \times$ BPF (121 Hz) is summarized in Table 4, whereas the noise control performance is given in Table 5. The vibration suppression performance at this frequency, as indicated by the average acceleration values (i.e., the sensed variables), the individual accelerometer signals, and the rms value of

all 12 accelerometers were slightly reduced when compared to the BPF. Nevertheless, the reduction in vibration provided by the control system was still impressive. However, the accompanying noise control performance was significantly poorer than at the BPF, resulting, in fact, in a marginally higher overall noise level (i.e., by 1.6 dB). The reason for this is ultimately traceable to the greater number of structural and acoustic modes interacting at this higher frequency. With the greater complexity of the structural-acoustic coupling, it is probable that the mode which dominates the vibration field couples poorly with the mode that dominates the interior acoustic field. This situation would result in an essentially unaltered acoustic field even if the dominant vibration mode were effectively suppressed. When configuration B (i.e., with acoustic sensing) was tested in the presence of the 2 × BPF disturbance, the noise control performance was only marginally better than configuration A (see Table 5). Here the overall rms noise level increased by 0.7 dB. The three control microphones did exhibit a modest rms reduction of 1.8 dB. Upon closer examination of the operating deflection shape (ODS) at 2 × BPF (121 Hz), it was realized that with configuration A or B the lower end of the actuator was located at a position that leads to unfavorable coupling with the 121 Hz ODS (see Fig. 10) and therefore provided ineffective suppression of this ODS. An alternate actuator configuration, denoted C, was developed to improve suppression of the 2 × BPF (121 Hz) ODS while providing effective suppression of BPF ODS.

For configuration C the piezoelectric elements between adjacent nodal points at 2 × BPF (denoted as IV and II in Fig. 10) at *all* three axial locations were grouped together to form one actuator, whereas the elements between points II and III at all three axial locations formed a second actuator. Configuration C is also shown in Fig. 11, where piezo elements p16–p49 on all three frames are grouped together to form the first actuator, whereas the elements from p50 to p68 on all three frames are grouped to form the second actuator. This configuration provided a more effective suppression of the 2 × BPF than configuration A at the price of reduced suppression of the ODS at the BPF. The lack of piezoelectric elements precluded the coverage from extending beyond point III. Had this been possible, one would expect even higher controllability over the vibration fields at both the BPF and 2 × BPF. In this case six accelerometers between points IV and II (two per axial location) were averaged to form two effective error sensors, whereas another six between II and III (also two per axial location) were averaged to form another pair of sensors. This configuration is also shown in Fig. 11, where the four velocity sensors were formed by averaging signals from accelerometers: a1, a5, and a9 for sensor I; a2, a6, and a10 for sensor II; a3, a7,

Table 4 Vibration attenuation in decibels at 121 Hz, vibration sensing, configuration A

Accelerometer	Location	Attenuation, dB
a1	Lower, frame 1	−7
a2	Frame 1	9
a3	Frame 1	13
a4	Upper, frame 1	8
Sensor I (average: a1–a4)	——	20
a5	Lower, frame 2	−4
a6	Frame 2	15
a7	Frame 2	14
a8	Upper, frame 2	10
Sensor II (average: a5–a8)	——	20
a9	Lower, frame 3	−1
a10	Frame 3	14
a11	Frame 3	7
a12	Upper, frame 3	1
Sensor III (average: a9–a12)	——	21
rms: a1–a12	——	5.7

Table 5 Interior noise attenuation in decibels at 121 Hz, configuration A and B

Microphone	Location	Configuration A (accelerometer sensing)	Configuration B (microphone sensing)
m1	Row 1, window seat	−2	−2
m2	Row 1, aisle seat	−2	−4
m3	Row 1, standing aisle	−3	−1
m4	Row 2, window seat	5	4
m5	Row 2, aisle seat	−1	−1
m6	Row 2, standing aisle	−1	2
m7	Row 3, window seat	−1	1
m8	Row 3, aisle seat	−3	−1
m9	Row 3, standing aisle	−2	−1
Average: m1–m9	——	−1.1	−0.49
rms: m1–m9	——	−1.6	−0.7

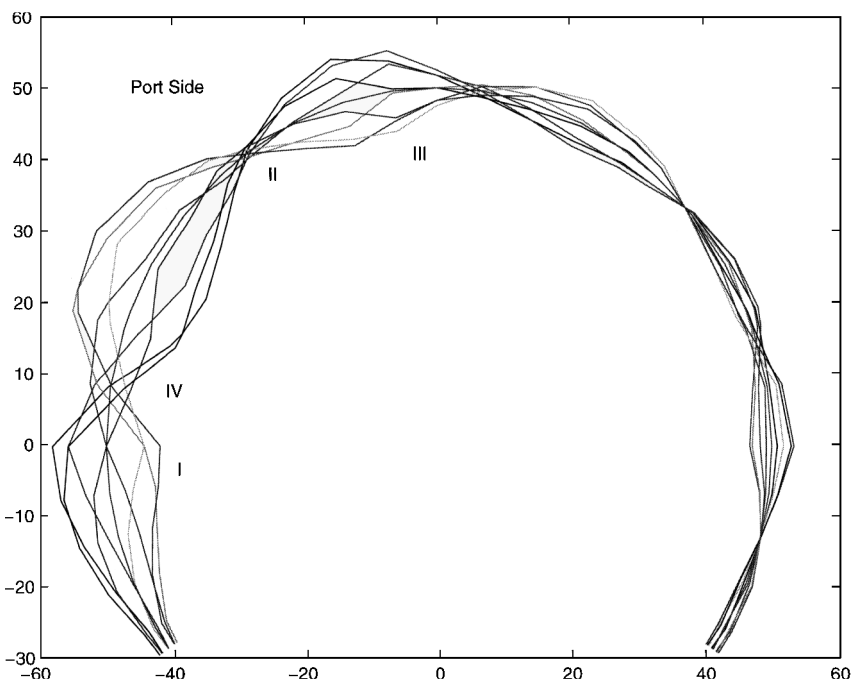

Fig. 10 Measured operating deflection shape as a result of simulated propeller noise, 2 × BPF, 910 rpm (121 Hz).

Table 6 Vibration attenuation in decibels at 61 Hz, vibration sensing, actuator/sensor configuration C

Accelerometer	Location	Vibration attenuation, dB
a1	Lower, frame 1	6
a2	Frame 1	13
a3	Frame 1	8
a4	Upper, frame 1	33
a5	Lower, frame 2	8
a6	Frame 2	11
a7	Frame 2	11
a8	Upper, frame 2	18
a9	Lower, frame 3	5
a10	Frame 3	11
a11	Frame 3	13
a12	Upper, frame 3	22
rms: a1–a12	——	9.9

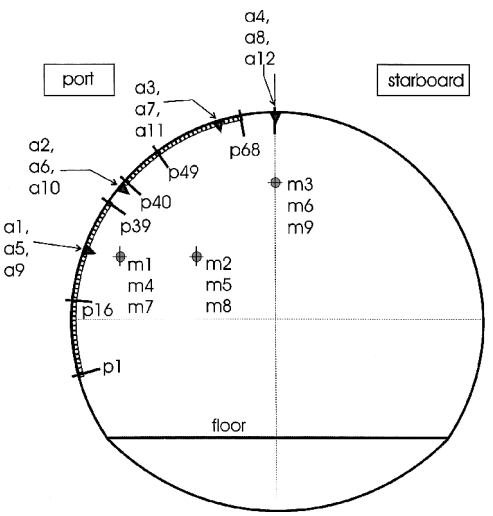

Fig. 11 Section through frame 1, showing accelerometer positions (a1 to a12) for configuration C.

and a11 for sensor III; and a4, a8, and a12 for sensor IV. The plant was modeled using an IIR filter with 15 forward and 14 recursive coefficients, whereas a FIR filter with 15 forward coefficients was used for the control filter. In this case plant identification was also carried out off-line. The achieved vibration reduction was again significant at the BPF (see Table 6). The vibration reduction performance was only slightly reduced compared to the performance for configuration A at this frequency (9.9 dB vs 10.2 dB in rms reduction for all 12 accelerometers). However, the noise reduction performance (see Table 7) diminished from an overall tone-level rms reduction of 7.2 dB with configuration A to 3.4 dB with configuration C at the BPF. Furthermore, there were three microphone locations that exhibited slight increases in noise levels. Nevertheless, the overall noise reduction performance of this configuration was quite good. Next, the performance of this configuration in the presence of the $2 \times$ BPF (121 Hz) disturbance was assessed. The vibration attenuation performance, which is summarized in Table 8, indicates that configuration C is capable of reducing the level of vibration significantly at this frequency; the rms reduction over the 12 accelerometers was almost 8 dB. The level of noise reduction obtained with configuration C, shown in Table 9, is lower at $2 \times$ BPF than at the BPF, with the overall RMS noise level attenuated by only 1 dB.

When noise reduction is the only performance metric or criterion, the results obtained using microphone error sensing will generally be superior to those for vibration sensing. For example, with the identical actuator design as configuration C, but using the three microphones in seat row 2 as the error sensors, control at 61 and 121 Hz was explored. This will be referred to as configuration D.

Table 7 Interior noise attenuation in decibels at 61 Hz, configurations C and D

Microphone	Location	Configuration C (accelerometer sensing)	Configuration D (microphone sensing)
m1	Row 1, window seat	−3	2
m2	Row 1, aisle seat	7	10
m3	Row 1, standing aisle	7	12
m4	Row 2, window seat	−2	8
m5	Row 2, aisle seat	4	15
m6	Row 2, standing aisle	8	26
m7	Row 3, window seat	−2	3
m8	Row 3, aisle seat	2	11
m9	Row 3, standing aisle	6	13
Average: m1–m9	——	3.0	11.0
rms: m1–m9	——	3.4	10.6

Table 8 Vibration attenuation in decibels at 121 Hz, vibration sensing, configuration C

Accelerometer	Location	Vibration attenuation, dB
a1	Lower, frame 1	13
a2	Frame 1	10
a3	Frame 1	4
a4	Upper, frame 1	4
a5	Lower, frame 2	14
a6	Frame 2	13
a7	Frame 2	14
a8	Upper, frame 2	9
a9	Lower, frame 3	5
a10	Frame 3	23
a11	Frame 3	−2
a12	Upper, frame 3	10
rms: a1–a12	——	7.9

Table 9 Interior noise attenuation in decibels at 121 Hz, configurations C and D

Microphone	Location	Configuration C (accelerometer sensing)	Configuration D (microphone sensing)
m1	Row 1, window seat	5	4
m2	Row 1, aisle seat	4	6
m3	Row 1, standing aisle	−2	10
m4	Row 2, window seat	13	17
m5	Row 2, aisle seat	−1	9
m6	Row 2, standing aisle	−1	2
m7	Row 3, window seat	7	11
m8	Row 3, aisle seat	2	4
m9	Row 3, standing aisle	0	6
Average: m1–m9	——	3.1	7.8
rms: m1–m9	——	1.0	6.8

IIR filters with 15 forward and 14 recursive coefficients were used both to model the plant and to implement the controller. Once again, off-line RLMS identification of the secondary path of the plant was performed. The results for the BPF, which are given in the last column of Table 7, demonstrate the superiority in the noise reduction performance; the RMS attenuation over all microphone locations was more than 10 dB (7 dB greater than in the case when accelerometer error sensing was employed). At 121 Hz noise control performance using microphone sensing was again much better than with accelerometer sensing, with the rms reduction over all nine microphones being almost 7 dB (i.e., 6 dB greater than in configuration C). In both these cases (61 and 121 Hz) the reductions were global in nature for configuration D.

Conclusions

The use of adaptive feedforward control in an ASAC setting was applied successfully to reduce interior noise and vibration in a full-scale aircraft fuselage subjected to simulated propeller noise at multiple frequencies in laboratory testing. This was achieved using a control system that incorporated segmented piezoelectric actuators bonded to the fuselage and either acoustic or vibration error sensing.

The results of this investigation demonstrated that through judicious actuator and sensor design considerations, which were outlined, ASAC systems using bonded piezoelectric actuators and accelerometers were capable of simultaneously providing significant noise reduction and vibration suppression in the passenger cabin of aircraft subjected to simulated propeller noise. Optimization for a single, low-frequency disturbance resulted in excellent noise reduction at that frequency, but poor performance at higher frequencies. However, the same actuator design methodology was applied for control at two operating frequencies and resulted in reasonable performance at both frequencies when vibration sensing is employed. When microphone sensing was used instead, noise reduction increased dramatically, providing over 10 dB (rms) and almost 7 dB (rms) of noise reduction, respectively at the BPF and 2 × BPF. Furthermore, the reductions were global in nature.

Acknowledgments

The contributions of Lacramioara Pavel and Michael Baranowski and Luc Hurtubise of the National Research Council of Canada and of Weiping Xu of Carleton University to this investigation are greatly appreciated.

References

[1]Mixson, J. S., and Powell, C. A., "Review of Recent Research on Interior Noise of Propeller Aircraft," AIAA Paper 84-2349, Oct. 1984.

[2]Lord, H. W., Gatley, W. S., and Evensen, H. A., *Noise Control for Engineers*, Krieger, Malabar, FL, 1980, pp. 258–263.

[3]Elliot, S. J., Nelson, P. A., Stothers, I. M., and Boucher, C. C., "In-Flight Experiments on the Active Control of Propeller-Induced Cabin Noise," *Journal of Sound and Vibration*, Vol. 140, No. 2, 1990, pp. 219–238.

[4]Warner, J. V., and Bernhard, R. J., "Digital Control of Local Sound Fields in an Aircraft Passenger Compartment," *AIAA Journal*, Vol. 28, No. 2, 1990, pp. 284–289.

[5]Silcox, R. J., Fuller, C. R., and Lester, H. C., "Mechanisms of Active Control in Cylindrical Fuselage Structures," *AIAA Journal*, Vol. 28, No. 8, 1990, pp. 1397–1404.

[6]Rossetti, D. J., Norris, M. A., Southward, S. C., and Sun, J. Q., "A Comparison of Speakers and Structural-Based Actuators for Aircraft Cabin Noise Control," *Proceedings of the Second Conference on Recent Advances in Active Control of Sound and Vibration*, edited by R. A. Burdisso, Technomic Pub. Co., Lancaster, PA, 1993, pp. S1–S10.

[7]Grewal, A., Nitzsche, F., Zimcik, D. G., and Leigh, B., "Active Control of Aircraft Cabin Noise Using Collocated Structural Actuators and Sensors," *Journal of Aircraft*, Vol. 35, No. 2, 1998, pp. 324–331.

[8]Grewal, A., Zimcik, D. G., Hurtubise, L., and Leigh, B., "Active Noise and Vibration Control of Turboprop Aircraft Using Multiple Piezoelectric Actuators," AIAA Paper 97-1638, May 1997.

[9]Widrow, B., and Stearns, S. D., *Adaptive Signal Processing*, Prentice–Hall, Upper Saddle River, NJ, 1985, pp. 99–114.

[10]Nelson, P. A., and Elliott, S. J., *Active Control of Sound*, Academic, London, 1992, pp. 387–396.

[11]"TMS320C4x User's Guide," Texas Instruments, Inc., Dallas, TX, Lit. SPRU063, March 1996.

[12]Xu, W., Afagh, F. F., Grewal, A., and Zimcik, D., "The Effects of Segmented Piezoelectric Actuator Configuration on Aircraft Noise Control Performance," AIAA Paper 98-1978, April 1998.

[13]Crawley, E. F., and de Luis, J., "Use of Piezoelectric Actuators as Elements of Intelligent Structures," *AIAA Journal*, Vol. 25, No. 11, 1987, pp. 1373–1385.

[14]Palumbo, D. L., and Padula, S. L., "Optimizing an Actuator Array for the Control of Multi-Frequency Noise in Aircraft Interiors," AIAA Paper 97-1615, May 1997.